
MACS: Multi-Agent Reinforcement Learning for Optimization of Crystal Structures

Elena Zamaraeva¹ Christopher M. Collins^{*1} George R. Darling^{*2} Matthew S. Dyer^{*1,2}

Bei Peng^{*3} Rahul Savani^{*,†,3,4} Dmytro Antypov¹ Vladimir V. Gusev³ Judith Clymo³

Paul G. Spirakis^{1,3} Matthew J. Rosseinsky^{1,2}

¹Leverhulme Research Centre for Functional Materials Design, University of Liverpool, UK

²Department of Chemistry, University of Liverpool, UK

³Department of Computer Science, University of Liverpool, UK

⁴The Alan Turing Institute, London, UK

Abstract

Geometry optimization of atomic structures is a common and crucial task in computational chemistry and materials design. Following the *learning to optimize* paradigm, we propose a new multi-agent reinforcement learning method called **Multi-Agent Crystal Structure optimization (MACS)** to address periodic crystal structure optimization. MACS treats geometry optimization as a partially observable Markov game in which atoms are agents that adjust their positions to collectively discover a stable configuration. We train MACS across various compositions of reported crystalline materials to obtain a policy that successfully optimizes structures from the training compositions as well as structures of larger sizes and unseen compositions, confirming its excellent scalability and zero-shot transferability. We benchmark our approach against a broad range of state-of-the-art optimization methods and demonstrate that MACS optimizes periodic crystal structures significantly faster, with fewer energy calculations, and the lowest failure rate.

1 Introduction

In computational chemistry, geometry optimization of an atomic structure is the process of finding a stable arrangement of atoms, following a sequence of displacements in a 3-dimensional space until a local energy minimum is reached [39]. Within geometry optimization, our focus in this paper is on crystal structures, which are characterized by their *periodicity*. The arrangement of atoms within a crystal directly determines its physical and chemical properties; hence the optimization of the crystal structure is crucial to the discovery of new crystalline materials and finds applications in electronics, energy applications, information storage, and other domains.

In fact, an entire field within materials design, known as crystal structure prediction (CSP), focuses on the computational prediction of stable crystal structures with desirable properties for subsequent synthesis in the laboratory [52, 53]. Significant effort in a CSP workflow is focused on exploring the potential energy surface (PES) and performing geometry optimizations on candidate structures to

*Equal contribution

†Corresponding author, e-mail: Rahul.Savani@liverpool.ac.uk

minimize the energy and local atomic forces. In this context, the key requirement for an optimization method is the ability to quickly produce a locally optimized equilibrium structure.

Existing approaches for geometry optimization of crystal structures include classical first- and second-order optimization methods such as the BroydenFletcherGoldfarbShanno (BFGS) algorithm [4, 14, 16, 40] and the Conjugate Gradient [41] method, as well as methods tailored to atomic structures such as the Fast Inertial Relaxation Engine (FIRE) [3]. However, these methods often require either a significant number of steps to optimize large structures or time-consuming calculations at each optimization step. This makes the time for optimization a bottleneck in applications that require thousands of local optimization runs, such as CSP.

In this work, we utilize the *learning to optimize* (L2O) paradigm [27, 8, 45] to improve the geometry optimization of crystal structures using *multi-agent reinforcement learning* (MARL). We observe that overall structural stability depends on the forces acting on individual atoms. The forces are partial derivatives (or gradients) of the energy with respect to atomic positions, and all forces are zero at equilibrium where the structure achieves a local energy minimum. Both the energy and the forces are mostly determined by each atom’s chemical properties and its surrounding local environment. Moreover, atoms of a given element, as well as those of chemically related elements, tend to adopt similar chemical local environments, resulting in multiple similar local environments in an optimized crystal structure. Hence, it is natural to consider individual atoms as agents, moving independently but simultaneously to collectively discover an overall structure that is stable, i.e., a local minimum of the energy landscape. We therefore formulate crystal structure geometry optimization as a MARL problem, with the aim of learning decentralized policies for individual atoms to collectively discover a locally optimized structure.

The energy (and most often forces) estimation is integrated in any optimization method, and various methods exist for this purpose. The available methods for computing energy/forces vary in their complexity and accuracy and, therefore, cost to compute. Lennard-Jones potentials (LJ) [26, 13] or the Miller-Brown surface [37, 35] are often used to model simple systems, while more complex methods, such as density functional theory (DFT), can estimate energies and forces for materials with high accuracy but at a very much greater computational cost. We utilize CHGNet [12], a machine learning interatomic potential model trained on DFT data, as it offers fast and accurate energy and gradient estimates for crystal structures.

In this work, we make the following contributions:

- To the best of our knowledge, we are the first to apply MARL to address periodic crystal structure optimization. Our proposed method, **Multi-Agent Crystal Structure optimization** (MACS), presents a novel formulation of periodic crystal structure optimization as a multi-agent coordination problem.
- Our extensive experiments demonstrate that MACS optimizes the crystal structures significantly more efficiently than a wide range of state-of-the-art methods. These experiments cover a diverse set of crystalline materials, including compositions with different elemental species, varying numbers of species, and distinct symmetry groups.
- MACS exhibits strong zero-shot transferability and scalability, maintaining efficiency in the optimization of larger structures from new, unseen compositions. Our work unlocks the potential of MARL for periodic crystal structure optimization.

2 Related Work

The L2O concept leverages machine learning to develop new optimization methods tailored to specific problems, and its application is rapidly expanding. This paradigm has been successfully applied to classical optimization challenges such as Bayesian swarm optimization [6], black-box optimization [9, 28], adversarial training [54], or partial differential equations solving [18].

The geometry optimization of atomic structures is also a target of the L2O concept. In [2], the authors propose a graph-based L2O approach to optimization of finite, non-periodic atomic clusters using the LJ and Calcium silicate hydrate potentials [33], as well as the Stillinger-Weber potentials (SW) [44]. The authors show that their method achieves lower energy in optimized clusters compared to FIRE, Adam [25], and Gradient Descent [43]. Another study [34] investigates the optimization of atomic clusters with LJ, SW, and Gupta potentials [19], focusing on the minimization of energy in the cluster.

Molecular optimization tasks, when the main objective is to achieve stable molecule configurations in the least number of steps, are explored in [36, 7, 1]. In [36], the authors utilize MARL to train the MolOpt optimizer and benchmark it against three baselines: BFGS, FIRE, and MDMin [23]. The findings in [36] indicate that the MolOpt optimizer surpasses MDMin, exhibits performance comparable to FIRE, and is inferior to that of BFGS. Despite differences in the design of the Markov Decision Process (MDP) and the application to distinct classes of chemical systems, we have added all baselines of [36] in our study to maintain consistency.

Reinforcement learning (RL) has also shown promise in other areas of computational chemistry, including the design of materials with specific properties [17, 24] and the optimization of the basin-hopping routine in CSP [56]. For a comprehensive overview of other applications of RL in chemistry, we direct the reader to the review in [42].

3 Preliminaries and Problem Formulation

3.1 Periodic Crystal Structures and Their Optimization

A crystal structure is characterized by its unit cell, typically, a parallelepiped, and the configuration of atoms within it. The unit cell repeats itself in all three dimensions, defining the infinite periodic arrangement of atoms (see Fig. 2a for a two-dimensional example).

Geometry or local optimization takes an initial structure as input and adjusts the positions of the atoms in the unit cell to achieve a structure where the energy is at a local minimum. An efficient procedure to perform geometry optimization is crucial due to its extensive usage throughout computational chemistry. Atomic configurations at a local minimum on the potential energy surface (PES) represent physically stable structures of a material, and thus the properties of a material commonly depend on these structures. Therefore, calculations of optoelectronic, vibrational, mechanical, and energetic properties will begin with geometry optimization to achieve a local minimum.

In the scope of crystal structure optimization, global and local optimization are distinguished by their targets. The global crystal structure optimization, which is the ultimate goal of CSP, aims to identify the global minimum energy structure for a given composition, representing the most stable configuration. However, achieving a globally optimal structure typically requires many iterations of structure generation or perturbation followed by local optimization [5, 55, 38, 48].

Geometry optimization terminates under two conditions. The first condition, termed the condition of success, requires the norm¹ of the maximum atomic forces within the structure to reach a specified threshold. We use the threshold 0.05 eV/Å, as it represents a typical use case in CSP applications [11]. The second condition, termed the condition of failure, occurs when the maximum allowable number of optimization steps is reached without satisfying the condition of success. We set the maximum number of steps to 1000, which is generally sufficient to optimize the structures within this work using state-of-the-art methods such as BFGS, BFGS with line search, or FIRE. Therefore, the problem of geometry optimization in our formulation is as follows.

Problem (geometry optimization): Given an initial crystal structure and the maximum of 1000 steps, to autonomously adjust the positions of the atoms in the fixed unit cell to locally minimize all atomic forces in the structure to below 0.05 eV/Å as quickly as possible.

3.2 Geometry Optimization as a Partially Observable Markov Game

We model geometry optimization of crystal structures as a partially observable Markov game (POMG) [32, 31]. POMG is a multi-agent extension of MDP, with partial observability introduced for each agent. This means that each agent has a private local observation of the global state of the environment. POMG can be represented by a tuple $\langle \mathbb{A}, \mathbb{S}, \mathbb{O}, \mathbb{U}, T, R_i \rangle$, where \mathbb{A} is a set of N agents; \mathbb{S} is the state space; $\mathbb{O} = \mathbb{O}_1 \times \dots \times \mathbb{O}_N$ is the joint observation space, where \mathbb{O}_i is the observation space of agent a_i ; $\mathbb{U} = \mathbb{U}_1 \times \dots \times \mathbb{U}_N$ is the joint action space, where \mathbb{U}_i is the action space of a_i ; R_i is the individual reward function that returns a scalar value to agent a_i for a transition

¹Throughout this paper, all vectors and atomic positions are expressed in Cartesian coordinates, with distances and vector norms defined by the L2 norm.

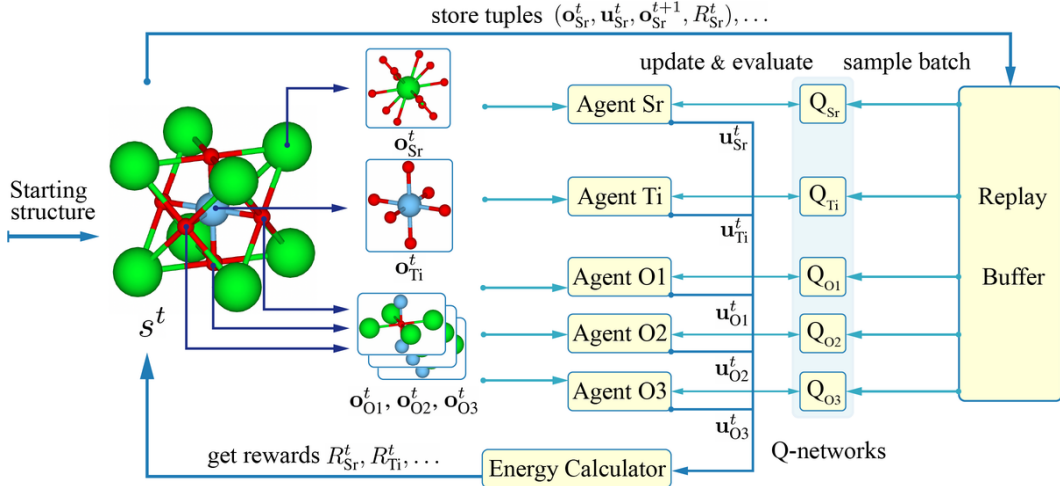


Figure 1: Our overall MACS architecture. We use the SrTiO_3 example with five atoms: one atom of Sr, one atom of Ti, and three atoms of O. At each time step t , the current state s^t is converted into individual observations $o_{\text{Sr}}^t, o_{\text{Ti}}^t, o_{\text{O1}}^t, o_{\text{O2}}^t, o_{\text{O3}}^t$ that are passed to the agent (policy) networks. The agent networks output individual actions, which are then scaled and used as the atoms’ displacements to update the structure. The energy calculator (CHGNet) provides the gradients for the updated structure to construct the next state s^{t+1} and compute the individual rewards. The policy training process follows the standard SAC [21] workflow with policy networks, Q-networks, and replay buffer.

from state $s \in \mathbb{S}$ to state $s' \in \mathbb{S}$ after taking joint action $u \in \mathbb{U}$; $T(s, u) : \mathbb{S} \times \mathbb{U} \rightarrow \mathbb{S}$ is the transition function, which determines the probability of transitioning to the next state $s' \in \mathbb{S}$ given that agents take joint action $u \in \mathbb{U}$ in state $s \in \mathbb{S}$. The transition function is deterministic in our problem setting.

By modelling the geometry optimization of crystal structures as a POMG, we treat each atom within a periodic unit cell of a structure as an individual agent, each with access to only local observations. All agents act independently and simultaneously to collectively discover a local minimum energy structure by maximizing their individual rewards. While each agent has a different reward function, they are aligned toward a common objective as optimizing the position of one atom improves the relative positions of the surrounding atoms. We impose partial observability intentionally to make the learning problem more tractable through the reasonable size of local observation spaces and to improve scalability to large numbers of atoms. The general scheme of MACS is presented in Fig. 1.

4 Methodology

In this section, we formally introduce the proposed formulation of periodic crystal structure optimization as a POMG through defining the observation space, action space, and reward function. Then we discuss our choice of the specific RL algorithm we use and its configuration.

Observations. Each atom in a crystal structure is surrounded by the neighboring atoms in the same unit cell, as well as their periodic images from the neighboring unit cells. Given this, we design the observation space so that each agent can observe its own features and the features of its k nearest neighbors. The k nearest neighbors refer to the k atoms closest to the agent and enumerated in the order of increasing distance, either within its unit cell or from their periodic images in the neighboring unit cells. Fig. 2a shows a two-dimensional example of k nearest neighbors of a specific atom in a structure.

To define the observation space, we start with defining the feature vector $\mathbf{f}_{a_i}^t$ of agent a_i at time step t :

$$\mathbf{f}_{a_i}^t = \text{concat}([r_i, c_i^t, \log(|\mathbf{g}_i^t|)], \mathbf{g}_i^t, \mathbf{d}_i^{t-1}, \mathbf{g}_i^t - \mathbf{g}_i^{t-1}). \quad (1)$$

Here concat is the concatenation function; r_i is the covalent radius of a_i , which does not change during optimization and serves both to distinguish between different species and to carry important

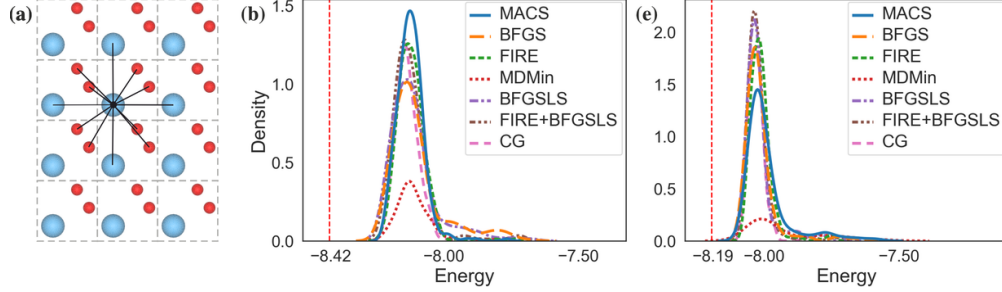


Figure 2: (a) Unit cells and nearest neighbors in two dimensions for a structure with three atoms. One atom is shown connected to its 12 nearest neighbors that belong to different unit cells; (b,c) The energy distribution of the local minima for the test sets of (b) SrTiO₃ with 80 atoms and (c) Ca₂Ti₃O₇ with 96 atoms. The vertical line indicates the energy of the experimental structure.

chemical information. The component c_i^t is the action scaling factor that will be explained when defining the action space. \mathbf{g}_i^t is the gradient vector of agent a_i at time step t , which is provided by CHGNet and scaled to avoid excessively large values (see Appendix A); $\log(|\mathbf{g}_i^t|)$ is used in the reward function and added to the feature vector to better capture the dependence of the reward on the observation. We call by *force-related* the features that use the gradient vector that directly indicates the stability of an atom and its local environment. $\mathbf{g}_i^t - \mathbf{g}_i^{t-1}$ is the change in the gradient vector from the previous time step t that reflects how successful the previous step was, and \mathbf{d}_i^{t-1} is the displacement of a_i at the previous time step $t - 1$; these are *history* features designed to reflect the optimization dynamics. The force-related and history features prove their significance for the policy efficiency in Section 5.4.

Now, we are ready to present the full observation of a_i at time step t as follows:

$$\mathbf{o}_{a_i}^t = \text{concat}(\mathbf{f}_{a_i}^t, \mathbf{f}_{n_{i1}^t}^t, \dots, \mathbf{f}_{n_{ik}^t}^t, [|\mathbf{r}_{i1}^t|, \dots, |\mathbf{r}_{ik}^t|], \mathbf{r}_{i1}^t, \dots, \mathbf{r}_{ik}^t). \quad (2)$$

Here, at time step t , $\mathbf{r}_{i1}^t, \dots, \mathbf{r}_{ik}^t$ are the relative (with respect to a_i) positions of k nearest neighbors of a_i , and $n_{i1}^t, \dots, n_{ik}^t$ are the agents occupying those positions. Relative positions of the agent's nearest neighbors and their feature vectors reflect the geometry and chemical properties of the agent's local environment. The observation design is illustrated by an example in Appendix A. In this study, we use the average-minimum-distance package [50, 49] for a fast construction of the k nearest neighbors and set $k = 12$; therefore, the observation vector has length 204.

Actions. A straightforward design for the action space would be to define actions as the agent's displacements. To ensure efficient learning, we propose using a scaling factor c_i^t that depends on the gradient vector norm (gnorm) of a_i at time step t to guide the order of magnitude of the action:

$$c_i^t = \min(|\mathbf{g}_i^t|, c_{max}). \quad (3)$$

Here c_{max} is a tunable hyperparameter (in this study, $c_{max} = 0.4$) to avoid excessively large steps. Given an action $\mathbf{u}_{a_i}^t \in [-1, 1]^3$ at time step t , the displacement of a_i is as follows:

$$\mathbf{d}_i^t = c_i^t \mathbf{u}_{a_i}^t. \quad (4)$$

The displacement can move an agent across the boundaries of the unit cell, in which case its position within the unit cell changes drastically. It is crucial that neither observation vectors nor action vectors use the positions of atoms within the unit cell, as this approach allows smooth crossing between unit cells and the handling of multiple neighbors corresponding to the same agent from different unit cells.

Rewards. The reward function should reflect the objective of reducing the atomic forces in a structure to sufficiently low values. Hence, we propose using the gnorms of a_i at the current timestep t and the next timestep $t + 1$ to construct the individual reward for a_i as follows:

$$R_{a_i}^t = \log(|\mathbf{g}_i^t|) - \log(|\mathbf{g}_i^{t+1}|). \quad (5)$$

The logarithmic term helps to avoid skewing the policy toward short-term gains in the early stages of optimization, given the significant difference in gnorms' magnitudes between non-optimized and optimized structures. We define an episode as the complete optimization of a structure and use the discount factor $\gamma = 0.995$ to encourage the policy to achieve the low forces more quickly.

Independent SAC. To train agents to collectively discover a locally optimized structure, we use independent Soft Actor-Critic (SAC), which extends SAC [21] from the single-agent to the multi-agent setting by treating all other agents as part of the environment. Hence, the multi-agent problem is decomposed into a collection of simultaneous single-agent problems that share the same environment. SAC is chosen for its sample efficiency and its use of entropy regularization, which helps prevent early convergence to suboptimal policies and promotes a balance between exploration and exploitation.

The MACS workflow with independent SAC is presented in Fig. 1. Given a structure, CHGNet is used to estimate the forces acting on the atoms. First, the gradient vectors are scaled, and then the local observation vectors are constructed and normalized. Although it may seem redundant to scale gradient vectors before normalization in the observations, this helps to preserve the gradient directions better and makes the training stable. The observation vectors are then passed on to the policy network. We use a standard SAC architecture proposed in [21] and implemented in RLlib [29], and utilize the policy network and the twin Q-networks shared between all agents for efficient training. The policy and Q-networks are two-layered MLPs with ReLU activation functions. The policy network outputs three pairs (mean, std) for the action vector, which are passed through the tanh squashing to match the action space limits. The tuples $\langle \mathbf{o}_{a_i}^t, \mathbf{u}_{a_i}^t, \mathbf{o}_{a_i}^{t+1}, R_{a_i}^t \rangle$ are stored in a replay buffer with a capacity of 10 million. The hyperparameter tuning details are provided in Appendix A.

5 Experiments

In this section, we benchmark MACS against a set of methods commonly used for geometry optimization. We train MACS across a diverse set of chemical systems and compare its performance against baselines using various evaluation metrics that assess the efficiency and reliability of the approach. We demonstrate the scalability and zero-shot transferability of our approach by applying the trained policy to optimize structures of unseen (larger) sizes within unseen compositions. Furthermore, we conduct ablation studies to investigate the influence of our observation space, action space, and reward function designs on the performance of MACS. Finally, we compare the results of optimization by MACS and the baselines through analyzing the energy distribution for the optimized structures.

5.1 Training and Testing Dataset Generation

We train MACS on a set of six diverse chemical compositions: Y_2O_3 [56], $\text{Cu}_{28}\text{S}_{16}$ [11], SrTiO_3 [10], $\text{Ca}_3\text{Ti}_2\text{O}_7$ [11], $\text{Ca}_3\text{Al}_2\text{Si}_3\text{O}_{12}$ [20], and $\text{K}_3\text{Fe}_5\text{F}_{15}$ [22]. These compositions vary in the number of elements (2–4) and in the number of atoms (5–80) required to describe their experimental structures. We generate training and testing structures using the Ab Initio Random Structure Searching package (AIRSS) [30]. During training, the initial pseudo random structures are generated on the fly with the condition of belonging to one of the training compositions with equal probability and having ~ 40 atoms with a reasonable volume (see Appendix B for more details). For every composition on which the policy is trained, we generate three test sets of 300 structures each, with the structures containing K, 1.5K, and 2K atoms, where K is the size of the structures used during training.

To demonstrate the transferability of MACS, we generate test sets for three new compositions that do not participate in the training process. Specifically, we select a composition from the training list, SrTiO_3 , and three from the same set of elements: Sr_2TiO_4 , $\text{Sr}_3\text{Ti}_2\text{O}_7$, and $\text{Sr}_4\text{Ti}_3\text{O}_{10}$. For each of these new compositions, we create two test sets: one with structures approximately the same size as training structures and the other with structures twice the size.

5.2 Baselines and Evaluation Metrics

We benchmark MACS against six baselines: **BFGS** is a quasi-Newton method that approximates the Hessian matrix based on gradient information; **BFGSLS** is a variation of BFGS with line search [51]; **FIRE** is a first-order method which is based on the molecular dynamics approach with additional velocity adjustments and adaptive time steps; **FIRE+BFGSLS** is a hybrid approach where up to 250 steps of FIRE are followed by up to 750 steps of BFGSLS to fine tune the structure [15, 11]; **MDMin** is a modification of the velocity-Verlet method with all masses of atoms equal to 1; **CG** stands for the conjugate gradient baseline, specifically, the Polak-Ribiere algorithm. All baselines are implemented in the Atomic Simulation Environment package (ASE) [23] or SciPy [47]. We allow the optimization of a structure to last up to 1000 steps or until the forces of all atoms are below the defined threshold.

A natural way to compare geometry optimization methods is by the time and number of steps required to optimize an initial configuration, hence our first two evaluation metrics are the mean number of steps among successful optimizations (N_{mean}) and the mean optimization time (T_{mean}). We observe that for BFGSLS and CG, the number of steps is not equal to the number of energy calculations, as each step in both algorithms can involve more than one energy calculation. As energy calculations contribute significantly to the optimization time, we also use the mean number of energy calculations among the successful optimizations (C_{mean}) as an evaluation metric. Finally, we take into account the failure rate (P_F) of each method to estimate their reliability.

Table 1: Performance comparison of MACS and the baselines on all test sets, covering T_{mean} , C_{mean} , N_{mean} , and P_F . The metrics N_{mean} and C_{mean} are presented either as a single value (if they are identical) or separated by a ; symbol (if they differ). The lowest values of T_{mean} , C_{mean} , and P_F are shown in bold. The standard errors and P_F per test set are provided in Appendix B.

Composition	N atoms	T_{mean} (sec)							$N_{\text{mean}} : C_{\text{mean}}$						
		MACS	BFGS	FIRE	MDFin	BFGSLS	FIRE+ BFGSLS	CG	MACS	BFGS	FIRE	MDFin	BFGSLS	FIRE+ BFGSLS	CG
Y ₂ O ₃	40	18	48	42	74	28	38	64	121	313	262	442	137 ; 185	252 ; 267	122 ; 543
	60	32	85	92	155	70	74	118	147	340	338	553	178 ; 281	324 ; 357	145 ; 642
	80	48	137	130	207	97	112	184	169	395	393	625	206 ; 307	360 ; 403	171 ; 754
Cu ₂₈ S ₁₆	44	29	62	47	116	54	47	81	150	293	257	543	147 ; 177	232 ; 242	158 ; 716
	66	51	112	88	205	60	79	147	186	355	307	633	176 ; 201	280 ; 291	198 ; 881
	88	74	175	120	315	110	117	275	230	414	392	745	213 ; 239	352 ; 365	283 ; 1269
SrTiO ₃	40	57	94	109	248	65	102	134	143	255	314	625	133 ; 190	276 ; 299	141 ; 572
	60	90	163	202	461	138	200	250	179	316	379	719	169 ; 255	321 ; 406	168 ; 681
	80	142	242	366	672	214	332	452	208	329	446	765	199 ; 317	355 ; 433	205 ; 837
Ca ₃ Ti ₂ O ₇	48	59	135	119	264	68	120	156	146	270	324	623	136 ; 185	284 ; 317	151 ; 618
	72	106	199	239	479	184	252	301	183	310	408	707	168 ; 249	335 ; 374	186 ; 756
	96	163	276	412	705	195	324	499	205	353	467	762	193 ; 267	369 ; 447	213 ; 876
K ₃ Fe ₅ F ₁₅	46	31	82	124	155	68	98	132	111	274	246	501	135 ; 178	246 ; 263	134 ; 602
	69	51	146	214	276	118	181	248	128	320	293	596	163 ; 259	299 ; 344	160 ; 720
	92	96	236	377	485	154	271	371	143	359	326	642	176 ; 236	353 ; 396	181 ; 815
Ca ₃ Al ₂ Si ₃ O ₁₂	40	117	127	226	585	167	190	307	209	189	307	700	141 ; 264	269 ; 311	147 ; 553
	60	237	266	389	1068	276	422	572	264	230	382	755	165 ; 296	316 ; 391	177 ; 669
	80	343	333	627	1279	400	627	958	317	246	461	894	189 ; 327	350 ; 458	214 ; 814
Compositions unseen during training															
Sr ₂ TiO ₄	56	65	145	174	361	105	139	234	172	335	371	700	162 ; 218	319 ; 353	175 ; 716
	112	189	358	665	759	414	440	559	245	420	554	850	242 ; 397	427 ; 508	245 ; 1003
Sr ₃ Ti ₂ O ₇	48	54	123	151	315	88	130	191	153	288	345	676	153 ; 210	299 ; 323	167 ; 682
	96	159	369	497	800	366	375	477	227	382	501	817	212 ; 343	385 ; 449	223 ; 909
Sr ₄ Ti ₃ O ₁₀	34	30	77	87	174	48	76	106	126	251	282	547	124 ; 173	256 ; 275	137 ; 557
	68	113	202	238	498	149	205	307	186	310	408	729	179 ; 304	339 ; 385	183 ; 743
AVERAGE ²	66	99	175	239	444	152	207	297	182	315	366	673	171 ; 253	317 ; 361	179 ; 747
P_F (%)		0.36	3	9.64	46.19	0.36	0.82	18.22							

² The average is taken as the average across the metric values for all tests, i.e. the mean of the column above.

5.3 MACS Policy Evaluation

We train MACS for ~ 80000 steps in total. After training, we optimize the structures of the test sets with MACS and the baselines using the same hardware but allowing the usage of exactly one CPU for each optimization (see Appendix B for more details).

Tab. 1 shows the optimization results of MACS and the baselines across all test sets, covering the four evaluation metrics (T_{mean} , N_{mean} , C_{mean} , and P_F) mentioned above. We observe that MACS is substantially faster and requires fewer energy calculations than all baselines in nearly all test sets, with only a few exceptions. Specifically, on average, T_{mean} and C_{mean} of MACS are 34% and 28% less than those of the best baseline, BFGSLS, respectively. We can also see that MACS has the lowest failure rate ($P_F = 0.36\%$) and performs comparably to BFGSLS on this metric. In terms of N_{mean} , BFGSLS performs slightly better than MACS, requiring 5% fewer steps on average. MACS performs comparably to CG and outperforms all other baselines. However, CG has a much higher failure rate ($P_F = 18.22\%$) than MACS. Both BFGSLS and CG involve multiple energy calculations per step, resulting in more total energy calculations and longer optimization time compared to MACS.

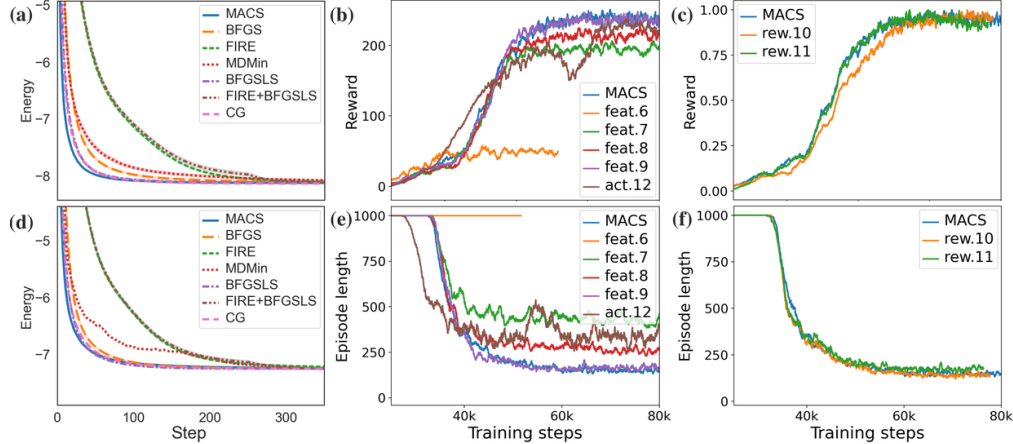


Figure 3: (a, d) Energy evolution averaged over all successfully optimized structures of 80 atoms within compositions SrTiO_3 (a) and $\text{Ca}_3\text{Al}_2\text{Si}_3\text{O}_{12}$ (d); (b,c,e,f) The ablation studies: the discounted episodic reward (b, e) and the mean episode length (c, f) across all compositions during training for MACS and its modifications.

MACS consistently outperforms all baselines in \mathbf{T}_{mean} and \mathbf{C}_{mean} across all compositions and structure sizes, except for $\text{Ca}_3\text{Al}_2\text{Si}_3\text{O}_{12}$, where MACS ranks first or second after BFGS. This demonstrates the scalability of our method, as it maintains competitive performance as the structure size increases. Moreover, MACS exhibits excellent zero-shot transferability, as it outperforms all baselines in \mathbf{T}_{mean} and \mathbf{C}_{mean} in all sets of structures of compositions on which it was not trained.

Figs. 2b and 2c show the energy distributions for local minima obtained by different methods. We can see that, when optimizing the same set of structures, MACS and the baselines sample from the same distribution of local minima. Figs. 3a and 3d show the energy evolution averaged over all successful optimizations for the test sets of the SrTiO_3 and $\text{Ca}_3\text{Al}_2\text{Si}_3\text{O}_{12}$ structures containing 80 atoms. It demonstrates that MACS decreases energy faster than the baselines or performs comparably to the best ones among them.

5.4 Ablation Studies

We compare the MACS design proposed in Section 4 (referred to as MACS) with its modifications.

Observations. We perform ablation experiments to investigate the influence of the feature representation in the observation space on our method’s performance. Specifically, we compare the MACS atom feature vector provided in Eq. 1 with the feature vectors in Eqs. 6 to 9 (referred to as feat.6, feat.7, feat.8, or feat.9), which use reduced feature representations that exclude some force-related or history features. For all setups, we evaluate the mean episodic reward and the mean episode length achieved by them across all compositions during training. As shown in Figs. 3b and 3e, MACS and feat.9 achieve the best performance, while feat.6 shows the worst performance. This demonstrates the importance of including force-related features in the observation space. We then evaluate the policies trained with different feature designs on optimizing the SrTiO_3 composition from the test sets. Tab. 2 shows that MACS performs substantially better than feat.7 and feat.8 in \mathbf{T}_{mean} and \mathbf{N}_{mean} . The design feat.9 shows marginally lower performance in \mathbf{N}_{mean} and better performance in \mathbf{T}_{mean} compared to MACS. In Appendix B, we further evaluate feat.9 on all remaining test sets and see that it takes on average $\sim 7.7\%$ more optimization steps than MACS. These results show that both force-related and history features are crucial to the competitive performance of MACS.

$$\mathbf{f}_{a_i}^t = \text{concat}([r_i, c_i^t, \mathbf{d}_i^{t-1}], \mathbf{g}_i^t), \quad (6)$$

$$\mathbf{f}_{a_i}^t = \text{concat}([r_i, c_i^t, \log(|\mathbf{g}_i^t|)], \mathbf{g}_i^t), \quad (7)$$

$$\mathbf{f}_{a_i}^t = \text{concat}([r_i, c_i^t, \log(|\mathbf{g}_i^t|)], \mathbf{g}_i^t, \mathbf{g}_i^t - \mathbf{g}_i^{t-1}), \quad (8)$$

$$\mathbf{f}_{a_i}^t = \text{concat}([r_i, c_i^t, \log(|\mathbf{g}_i^t|)], \mathbf{g}_i^t, \mathbf{d}_i^{t-1}). \quad (9)$$

Rewards. To investigate the influence of the reward function on the performance of our method, we explore two additional reward designs. For the first reward design (rew.10), we add a fixed *penalty*

(tuned to -0.05) at each step to the reward used in Eq. 5, to explore whether this encourages faster optimization:

$$R_{a_i}^t = \log(|\mathbf{g}_i^t|) - \log(|\mathbf{g}_i^{t+1}|) + \textit{penalty}. \quad (10)$$

Table 2: Performance comparison of MACS with varying feature representations (feat.7-9) in the observation space and varying reward functions (rew.10,11). The best numbers are shown in bold. The design feat.6 is excluded due to its inability to successfully optimize structures.

Composition	N atoms	\mathbf{T}_{mean} (sec)						\mathbf{N}_{mean}					
		MACS	feat.7	feat.8	feat.9	rew.10	rew.11	MACS	feat.7	feat.8	feat.9	rew.10	rew.11
SrTiO ₃	40	57	146	79	46	50	54	143	416	256	145	144	169
	60	90	242	147	82	88	83	179	504	303	184	187	202
	80	142	385	236	132	154	161	208	572	373	209	220	239
AVERAGE	60	96	258	154	87	97	99	177	498	311	180	184	204
\mathbf{P}_F (%)		0.22	8.11	0.44	0.44	0	0.33						

The second reward design (rew.11) explores the effects of partial reward sharing by adding the average reward across all agents to the original individual reward used in Eq. 5:

$$R_{a_i}^t = \log(|\mathbf{g}_i^t|) - \log(|\mathbf{g}_i^{t+1}|) + \frac{1}{N} \sum_{j=1}^N (\log(|\mathbf{g}_j^t|) - \log(|\mathbf{g}_j^{t+1}|)). \quad (11)$$

Fig. 3c and 3f show the mean episodic reward and mean episode length achieved by our method with different reward functions. Note that the episodic reward is normalized to make performance comparable between different reward functions. We can see that rew.10 and rew.11 perform similarly to MACS. We then evaluate the policies trained with the three reward functions on optimizing the SrTiO₃ composition from the test sets. Tab. 2 shows that, MACS achieves superior performance than rew.10 and rew.11 in \mathbf{T}_{mean} and \mathbf{N}_{mean} on the test set with the largest structures (80 atoms).

Actions. We consider a straightforward action design (act.12) in which the action vector is used directly as atom’s displacement (without the scaling factor c_i^t as defined in Eq. 3):

$$\mathbf{d}_i^t = \mathbf{u}_{a_i}^t. \quad (12)$$

Fig. 3b shows that both action designs converge to similar episodic rewards, but act.12 is significantly less sample-efficient and stable. Moreover, Fig. 3e shows that act.12 converges to higher average episode length, resulting in more optimization steps. This demonstrates that the scaling factor introduced in our action design is crucial to the competitive performance of MACS, enabling more sample-efficient and stable learning.

6 Conclusion

In this work, we present MACS, a new MARL method for periodic crystal structure optimization. MACS introduces a novel model of geometry optimization as a multi-agent coordination problem, an unexplored direction that poses unique challenges in balancing expressive yet compact representations of chemical and geometric information, modelling complex atomic interactions, and enabling efficient, scalable policy learning. We conduct extensive experiments comparing MACS with various state-of-the-art methods and demonstrate that it learns a policy capable of efficiently optimizing crystal structures across a diverse set of test cases, significantly outperforming all baselines. We show that on average across all test sets, MACS optimizes the structures 34% faster and with 28% fewer energy calculations than the strongest baseline, BFGSLs, preserving the lowest failure rate.

MACS demonstrates scalability and zero-shot transferability, as it is superior to the baselines in the optimization of the structures of larger sizes and compositions that it does not encounter during training. In conclusion, MACS has the potential to become a universal geometric optimizer for periodic crystal structures.

Limitations and future work. In this study, the only feature that differentiates atomic species is the covalent radius. Various atomic features and existing descriptor implementations [57, 46] will

be considered in the future. The analysis of the observation space in Section 5.4 confirmed that the history plays a crucial role in the efficiency of the method. Hence, the integration of recurrent neural networks into the method could improve MACS, and we will investigate this matter further. Another promising direction for future work is learning to optimize the unit cell of the structure. We plan to treat the unit cell vectors as separate agents, optimizing them in a manner similar to the way atoms optimize their positions. Finally, alternative ways to estimate the energy of structures can be used to replace CHGNet. In particular, DFT is of interest as the most accurate energy estimator among existing methods. As CHGNet is trained on DFT, the train-with-CHGNet-run-with-DFT workflow presents a promising concept for future study.

7 Acknowledgements

The authors would like to thank Professor Igor Potapov who gave valuable feedback that improved the quality of our work.

The authors acknowledge funding from the Leverhulme Trust via the Leverhulme Research Centre for Functional Materials Design. For the purpose of open access, the authors have applied a Creative Commons Attribution (CC BY) license to any Author Accepted Manuscript version arising from this submission.

References

- [1] Kabir Ahuja, William H Green, and Yi-Pei Li. Learning to optimize molecular geometries using reinforcement learning. *Journal of Chemical Theory and Computation*, 17(2):818–825, 2021.
- [2] Vaibhav Bihani, Sahil Manchanda, Srikanth Sastry, Sayan Ranu, and NM Anoop Krishnan. Stridernet: A graph reinforcement learning approach to optimize atomic structures on rough energy landscapes. In *International Conference on Machine Learning*, pages 2431–2451. PMLR, 2023.
- [3] Erik Bitzek, Pekka Koskinen, Franz Gähler, Michael Moseler, and Peter Gumbsch. Structural relaxation made simple. *Physical review letters*, 97:170201, 2006.
- [4] Charles George Broyden. The convergence of a class of double-rank minimization algorithms 1. general considerations. *IMA Journal of Applied Mathematics*, 6(1):76–90, 1970.
- [5] Christian J Burnham and Niall J English. Crystal structure prediction via basin-hopping global optimization employing tiny periodic simulation cells, with application to water–ice. *Journal of Chemical Theory and Computation*, 15(6):3889–3900, 2019.
- [6] Yue Cao, Tianlong Chen, Zhangyang Wang, and Yang Shen. Learning to optimize in swarms. *Advances in neural information processing systems*, 32, 2019.
- [7] Yu-Cheng Chang and Yi-Pei Li. Integrating chemical information into reinforcement learning for enhanced molecular geometry optimization. *Journal of Chemical Theory and Computation*, 19(23):8598–8609, 2023.
- [8] Tianlong Chen, Xiaohan Chen, Wuyang Chen, Howard Heaton, Jialin Liu, Zhangyang Wang, and Wotao Yin. Learning to optimize: A primer and a benchmark. *Journal of Machine Learning Research*, 23(189):1–59, 2022.
- [9] Yutian Chen, Matthew W Hoffman, Sergio Gómez Colmenarejo, Misha Denil, Timothy P Lillicrap, Matt Botvinick, and Nando Freitas. Learning to learn without gradient descent by gradient descent. In *International Conference on Machine Learning*, pages 748–756. PMLR, 2017.
- [10] Christopher M Collins, George R Darling, and Matthew J Rosseinsky. The flexible unit structure engine (fuse) for probe structure-based composition prediction. *Faraday Discussions*, 211:117–131, 2018.
- [11] Christopher M Collins, Hasan M Sayeed, George R Darling, John B Claridge, Taylor D Sparks, and Matthew J Rosseinsky. Integration of generative machine learning with the heuristic crystal structure prediction code fuse. *Faraday Discussions*, 256:85–103, 2025.

- [12] Bowen Deng, Peichen Zhong, Kyujung Jun, Janosh Riebesell, Kevin Han, Christopher J Bartel, and Gerbrand Ceder. CHGNet as a pretrained universal neural network potential for charge-informed atomistic modelling. *Nature Machine Intelligence*, 5(9):1031–1041, September 2023.
- [13] Jonathan PK Doye, Mark A Miller, and David J Wales. The double-funnel energy landscape of the 38-atom lennard-jones cluster. *The Journal of Chemical Physics*, 110(14):6896–6906, 1999.
- [14] Roger Fletcher. A new approach to variable metric algorithms. *The Computer Journal*, 13(3):317–322, 1970.
- [15] Julian D Gale and Andrew L Rohl. The general utility lattice program (gulp). *Molecular Simulation*, 29(5):291–341, 2003.
- [16] Donald Goldfarb. A family of variable-metric methods derived by variational means. *Mathematics of computation*, 24(109):23–26, 1970.
- [17] Prashant Govindarajan, Santiago Miret, Jarrid Rector-Brooks, Mariano Phielipp, Janarthanan Rajefndran, and Sarath Chandar. Learning conditional policies for crystal design using offline reinforcement learning. *Digital Discovery*, 3(4):769–785, 2024.
- [18] Daniel Greenfeld, Meirav Galun, Ronen Basri, Irad Yavneh, and Ron Kimmel. Learning to optimize multigrid pde solvers. In *International Conference on Machine Learning*, pages 2415–2423. PMLR, 2019.
- [19] Raju P Gupta. Lattice relaxation at a metal surface. *Physical Review B*, 23(12):6265, 1981.
- [20] Vladimir V Gusev, Duncan Adamson, Argyrios Deligkas, Dmytro Antypov, Christopher M Collins, Piotr Krysta, Igor Potapov, George R Darling, Matthew S Dyer, Paul Spirakis, and Matthew J Rosseinsky. Optimality guarantees for crystal structure prediction. *Nature*, 619(7968):68–72, 2023.
- [21] Tuomas Haarnoja, Aurick Zhou, Pieter Abbeel, and Sergey Levine. Soft actor-critic: Off-policy maximum entropy deep reinforcement learning with a stochastic actor. In *International Conference on Machine Learning*, pages 1861–1870. PMLR, 2018.
- [22] Anne-Marie Hardy, Antoine Hardy, and Gérard Ferey. Structure cristalline du bronze pseudo-quadratique $K_{0.6}FeF_3$: transition pyrochlore-quadratique pour les composés $KMM'X_6$. *Acta Crystallographica Section B*, 29(8):1654–1658, Aug 1973.
- [23] Ask Hjorth Larsen, Jens Irgen Mortensen, Jakob Blomqvist, Ivano E Castelli, Rune Christensen, Marcin Duak, Jesper Friis, Michael N Groves, Bjrk Hammer, Cory Hargus, Eric D Hermes, Paul C Jennings, Peter Bjerre Jensen, James Kermode, John R Kitchin, Esben Leonhard Kolsbjerg, Joseph Kubal, Kristen Kaasbjerg, Steen Lysgaard, Jn Bergmann Maronsson, Tristan Maxson, Thomas Olsen, Lars Pastewka, Andrew Peterson, Carsten Rostgaard, Jakob Schitz, Ole Schtt, Mikkel Strange, Kristian S Thygesen, Tejs Vegge, Lasse Vilhelmsen, Michael Walter, Zhenhua Zeng, and Karsten W Jacobsen. The atomic simulation environmenta python library for working with atoms. *Journal of Physics: Condensed Matter*, 29(27):273002, 2017.
- [24] Christopher Karpovich, Elton Pan, and Elsa A Olivetti. Deep reinforcement learning for inverse inorganic materials design. *npj Computational Materials*, 10(1):287, 2024.
- [25] Diederik P Kingma and Jimmy Ba. Adam: A method for stochastic optimization. *arXiv preprint arXiv:1412.6980*, 2014.
- [26] JE Lennard and I Jones. On the determination of molecular fields.i. from the variation of the viscosity of a gas with temperature. *Proceedings of the Royal Society of London. Series A, Containing Papers of a Mathematical and Physical Character*, 106(738):441–462, 1924.
- [27] Ke Li and Jitendra Malik. Learning to optimize. *arXiv preprint arXiv:1606.01885*, 2016.
- [28] Xiaobin Li, Kai Wu, Xiaoyu Zhang, and Handing Wang. B2opt: Learning to optimize black-box optimization with little budget. In *Proceedings of the AAAI Conference on Artificial Intelligence*, volume 39, pages 18502–18510, 2025.

- [29] Eric Liang, Richard Liaw, Robert Nishihara, Philipp Moritz, Roy Fox, Ken Goldberg, Joseph Gonzalez, Michael Jordan, and Ion Stoica. Rllib: Abstractions for distributed reinforcement learning. In *International Conference on Machine Learning*, pages 3053–3062. PMLR, 2018.
- [30] Leandro Liborio, Simone Sturniolo, and Dominik Jochym. Computational prediction of muon stopping sites using ab initio random structure searching (airss). *The Journal of Chemical Physics*, 148(13):134114, 2018.
- [31] Michael L Littman. Markov games as a framework for multi-agent reinforcement learning. In William W Cohen and Haym Hirsh, editors, *Machine Learning Proceedings 1994*, pages 157–163. Morgan Kaufmann, San Francisco (CA), 1994.
- [32] Ryan Lowe, YI WU, Aviv Tamar, Jean Harb, OpenAI Pieter Abbeel, and Igor Mordatch. Multi-agent actor-critic for mixed cooperative-competitive environments. In I. Guyon, U. Von Luxburg, S. Bengio, H. Wallach, R. Fergus, S. Vishwanathan, and R. Garnett, editors, *Advances in Neural Information Processing Systems*, volume 30. Curran Associates, Inc., 2017.
- [33] Enrico Masoero, E Del Gado, RJ-M Pellenq, F-J Ulm, and Sidney Yip. Nanostructure and nanomechanics of cement: polydisperse colloidal packing. *Physical review letters*, 109(15):155503, 2012.
- [34] Amil Merchant, Luke Metz, Samuel S Schoenholz, and Ekin D Cubuk. Learn2hop: Learned optimization on rough landscapes. In *International Conference on Machine Learning*, pages 7643–7653. PMLR, 2021.
- [35] Alexis W Mills, Joshua J Goings, David Beck, Chao Yang, and Xiaosong Li. Exploring potential energy surfaces using reinforcement machine learning. *Journal of Chemical Information and Modeling*, 62(13):3169–3179, 2022.
- [36] Rohit Modee, Sarvesh Mehta, Siddhartha Laghuvarapu, and U Deva Priyakumar. Molopt: Autonomous molecular geometry optimization using multiagent reinforcement learning. *The Journal of Physical Chemistry B*, 127(48):10295–10303, 2023.
- [37] Klaus Müller and Leo D Brown. Location of saddle points and minimum energy paths by a constrained simplex optimization procedure. *Theoretica chimica acta*, 53:75–93, 1979.
- [38] Artem R Oganov, Andriy O Lyakhov, and Mario Valle. How evolutionary crystal structure prediction works and why. *Accounts of chemical research*, 44(3):227–237, 2011.
- [39] H Bernhard Schlegel. Geometry optimization. *Wiley Interdisciplinary Reviews: Computational Molecular Science*, 1(5):790–809, 2011.
- [40] David F Shanno. Conditioning of quasi-newton methods for function minimization. *Mathematics of Computation*, 24(111):647–656, 1970.
- [41] Jonathan Richard Shewchuk et al. An introduction to the conjugate gradient method without the agonizing pain. *Technical report, Pittsburgh, PA, USA*, 1994.
- [42] Bhuvanesh Sridharan, Animesh Sinha, Jai Bardhan, Rohit Modee, Masahiro Ehara, and U Deva Priyakumar. Deep reinforcement learning in chemistry: A review. *Journal of Computational Chemistry*, 45(22):1886–1898, 2024.
- [43] Frank H Stillinger and Randall A LaViolette. Local order in quenched states of simple atomic substances. *Physical Review B*, 34(8):5136, 1986.
- [44] Frank H Stillinger and Thomas A Weber. Computer simulation of local order in condensed phases of silicon. *Physical review B*, 31(8):5262, 1985.
- [45] Ke Tang and Xin Yao. Learn to optimize – a brief overview. *National Science Review*, 11(8):nwae132, 2024.
- [46] Andriy Vasylenko, Dmytro Antypov, Sven Schewe, Luke M Daniels, John B Claridge, Matthew S Dyer, and Matthew J Rosseinsky. Digital features of chemical elements extracted from local geometries in crystal structures. *Digital Discovery*, 2025.

- [47] Pauli Virtanen, Ralf Gommers, Travis E Oliphant, Matt Haberland, Tyler Reddy, David Cournapeau, Evgeni Burovski, Pearu Peterson, Warren Weckesser, Jonathan Bright, et al. Scipy 1.0: fundamental algorithms for scientific computing in python. *Nature methods*, 17(3):261–272, 2020.
- [48] Junjie Wang, Hao Gao, Yu Han, Chi Ding, Shuning Pan, Yong Wang, Qiuhan Jia, Hui-Tian Wang, Dingyu Xing, and Jian Sun. Magus: machine learning and graph theory assisted universal structure searcher. *National Science Review*, 10(7):nwad128, 2023.
- [49] Daniel Widdowson and Vitaliy Kurlin. Resolving the data ambiguity for periodic crystals. In *Advances in Neural Information Processing Systems*, 2022.
- [50] Daniel Widdowson, Marco M Mosca, Angeles Pulido, Vitaliy Kurlin, and Andrew I Cooper. Average minimum distances of periodic point sets - foundational invariants for mapping periodic crystals. *MATCH Communications in Mathematical and in Computer Chemistry*, 87(3):529–559, 2022.
- [51] Philip Wolfe. Convergence conditions for ascent methods. ii: Some corrections. *SIAM Review*, 13(2):185–188, 1971.
- [52] Scott M Woodley and Richard Catlow. Crystal structure prediction from first principles. *Nature materials*, 7(12):937–946, 2008.
- [53] Scott M Woodley, Graeme M Day, and R Catlow. Structure prediction of crystals, surfaces and nanoparticles. *Philosophical Transactions of the Royal Society A*, 378(2186), 2020.
- [54] Yuanhao Xiong and Cho-Jui Hsieh. Improved adversarial training via learned optimizer. In *Computer Vision—ECCV 2020: 16th European Conference, Glasgow, UK, August 23–28, 2020, Proceedings, Part VIII 16*, pages 85–100. Springer, 2020.
- [55] Shiyue Yang and Graeme M Day. Exploration and optimization in crystal structure prediction: Combining basin hopping with quasi-random sampling. *Journal of Chemical Theory and Computation*, 17(3):1988–1999, 2021.
- [56] Elena Zamaraeva, Christopher M Collins, Dmytro Antypov, Vladimir V Gusev, Rahul Savani, Matthew S Dyer, George R Darling, Igor Potapov, Matthew J Rosseinsky, and Paul G Spirakis. Reinforcement learning in crystal structure prediction. *Digital Discovery*, 2(6):1831–1840, 2023.
- [57] Quan Zhou, Peizhe Tang, Shenxiu Liu, Jinbo Pan, Qimin Yan, and Shou-Cheng Zhang. Learning atoms for materials discovery. *Proceedings of the National Academy of Sciences*, 115(28):E6411–E6417, 2018.

A The MACS design and hyperparameter tuning

A.1 The nearest neighbors example

We consider a two-dimensional example of a structure with a square unit cell and three atoms a_1, a_2, a_3 , where a_2 and a_3 relate to the same chemical element. We assume that the structure is undergoing optimization, and Fig. 4 shows the atomic arrangement at time step t . Here, for agent a_1 , the first nearest neighbor is a periodic image of atom a_2 in a neighboring unit cell, hence $n_{11}^t = a_2$; the second nearest neighbor is a periodic image of a_3 in another neighboring unit cell, and the third nearest neighbor is atom a_3 itself, hence $n_{12}^t = n_{13}^t = a_3$. Furthermore, $\mathbf{r}_{11}^t, \mathbf{r}_{12}^t$, and \mathbf{r}_{13}^t denote the positions of the three nearest neighbors of a_1 , relative to a_1 , i.e. vectors in Euclidean space from a_1 to each of its three nearest neighbors. Therefore, the observation vector for agent a_1 at time step t looks as follows:

$$\mathbf{o}_{a_1}^t = \text{concat}(f_{a_1}^t, f_{a_2}^t, f_{a_3}^t, f_{a_3}^t, [|\mathbf{r}_{11}^t|, |\mathbf{r}_{12}^t|, |\mathbf{r}_{13}^t|], \mathbf{r}_{11}^t, \mathbf{r}_{12}^t, \mathbf{r}_{13}^t). \quad (13)$$

During the optimization process, the list of k nearest neighbors is updated at each time step: existing nearest neighbors may update their relative positions and ordering in the list, while some may leave the list and are replaced by new ones.

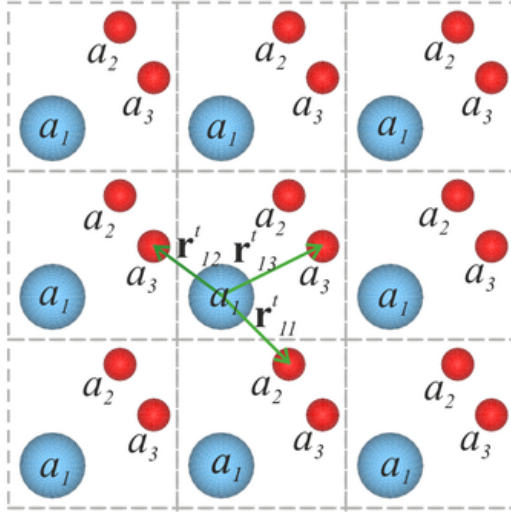


Figure 4: Two-dimensional structure with three atoms, and the three nearest neighbors for one of the atoms a_1 .

The amd package [50, 49] is used for the fast construction of the ordered list of the k nearest neighbors for all atoms on each step.

A.2 The number of nearest neighbors k

We explore the number of nearest neighbors that should be considered in the local observation of an agent. We choose 10, 12, and 15 nearest neighbors and train three policies using MACS that differ only in this hyperparameter. Fig. 5 shows that the three policies learned by MACS achieve comparable performance in both mean episodic reward and mean episode length during training. We then optimize the structures of the test sets of compositions Y_2O_3 , SrTiO_3 , and $\text{Ca}_3\text{Al}_2\text{Si}_3\text{O}_{12}$ with these policies. Table 3 shows that the policy with $k = 15$ has the highest failure rate and the longest optimization. The policies with $k = 10$ and $k = 12$ are comparable, with the latter being marginally better and therefore chosen for this study.

Table 3: Performance comparison of MACS with different numbers of nearest neighbors considered in agent’s local observation. The best number is in bold, the standard errors are in brackets.

Composition	N atoms	T_{mean} (sec)			N_{mean}		
		$k = 10$	$k = 12$	$k = 15$	$k = 10$	$k = 12$	$k = 15$
Y_2O_3	40	17(0)	18(1)	26(2)	123(2)	121(3)	137(4)
	60	34(1)	32(1)	48(3)	150(3)	147(3)	171(5)
	80	51(1)	48(1)	81(4)	179(4)	169(3)	201(6)
SrTiO_3	40	48(1)	57(12)	51(2)	148(3)	143(3)	164(4)
	60	76(2)	90(12)	88(2)	178(4)	179(4)	196(4)
	80	139(3)	142(13)	138(3)	215(5)	208(5)	232(5)
$\text{Ca}_3\text{Al}_2\text{Si}_3\text{O}_{12}$	40	124(4)	117(4)	148(6)	207(5)	209(5)	238(7)
	60	231(7)	237(14)	245(8)	274(7)	264(7)	307(8)
	80	380(11)	343(16)	436(13)	333(8)	317(8)	367(9)
AVERAGE	60	122	120	140	201	196	224
P_F (%)		0.56	0.78	3.52			

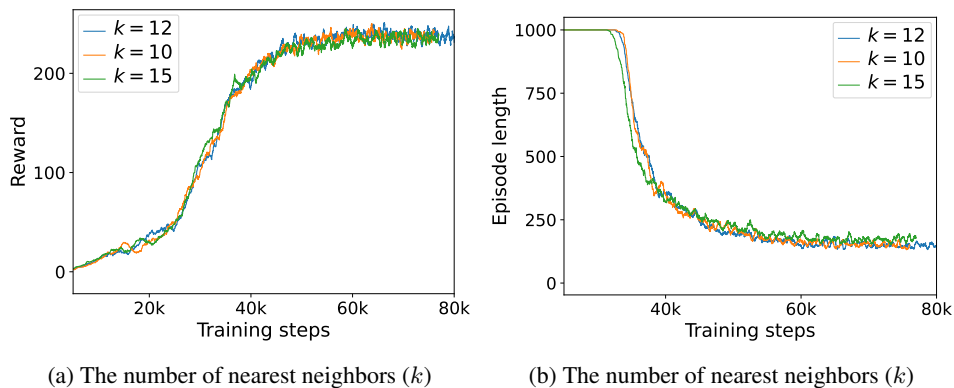


Figure 5: Mean episodic reward and mean episode length achieved by MACS with different numbers of nearest neighbors considered in agent’s local observation.

A.3 Gradient vector scaling

Let $\mathbf{g}_{o_i}^t$ be the gradient vector provided by CHGNet or any other energy/gradients calculator for agent a_i at time step t . The corresponding scaled gradient vector used for observations/actions/rewards in our study is calculated as follows:

$$\mathbf{G}_i^t = \begin{cases} \mathbf{g}_{o_i}^t, & \text{if } \|\mathbf{g}_{o_i}^t\|_\infty < g_{max}, \\ \mathbf{g}_{o_i}^t \times \frac{g_{max}}{\|\mathbf{g}_{o_i}^t\|_\infty}, & \text{otherwise.} \end{cases} \quad (14)$$

Here g_{max} is a tunable parameter. Our experiments showed that, while gradient vectors generally have components in the range $[-50, 50]$ at the beginning of optimization, occasionally there can be vectors with components up to 500. Such gradient vectors significantly unbalance training and eventually lead to gradient explosion (see Fig. 6). In practice, there is no difference between large and extremely large gradient vectors, as they all indicate a very undesirable atomic environment. Scaling the gradient vector to reasonable component values that preserve the direction helps mitigate this problem. Fig. 7 shows the mean episodic reward and the mean episode length achieved by MACS during training with different values of g_{max} . MACS with $g_{max} = 20$ converges to the highest reward, which is expected due to the higher gnorns at the beginning of the optimization, and hence, higher rewards. However, MACS with $g_{max} = 5$ converges to the lowest mean episode length while achieving high episodic reward, therefore, in this study, we use $g_{max} = 5$.

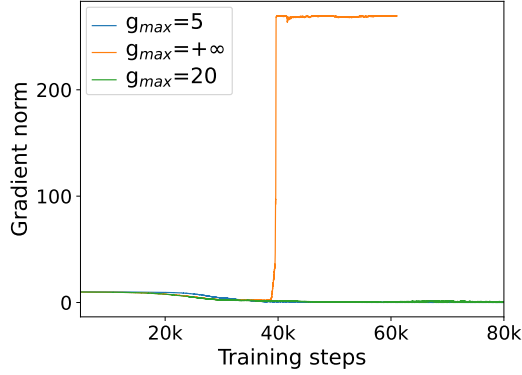


Figure 6: The gradient norm during training for MACS with different g_{max} .

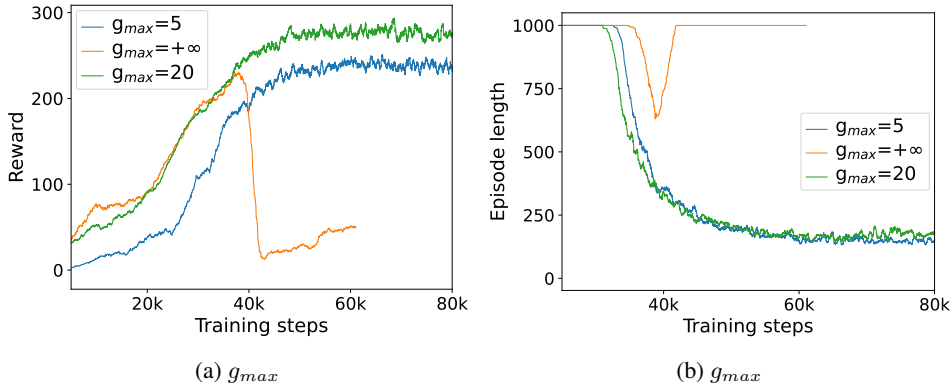


Figure 7: Performance comparison of MACS with different values of g_{max} .

A.4 Hyperparameter tuning for actions

The scaling factor c_i^t is applied for the action of agent a_i at time step t to guide the magnitude of the atom’s displacement. The upper boundary for c_i^t is defined by a hyperparameter c_{max} to avoid excessively large displacements. Fig. 8 compares two variants of c_{max} and shows that the smaller c_{max} allows the policy to converge to much higher mean episodic reward and lower episode length, and thus $c_{max} = 0.4$ was chosen for this study.

We also explore a straightforward approach for designing the action space: the action vector is used directly as the atom’s displacement (Eq. 12), without the scaling factor c_i^t . We consider different bounds on the action space to investigate its effect on policy learning, namely, we consider $[-a_{max}, a_{max}]^3$ for different values of a_{max} . We notice that, in SAC, the outputs of the policy network are tanh squashed and then scaled to fit the action space limits. It leads to different policy outputs’ magnitudes for the same action vector, depending on the action space limits. To take this into account, we also explore different values of the target entropy. We compare the mean episodic reward and the mean episode length achieved by MACS with different action space bounds and target entropy values. Fig. 9 shows that wider bounds on action space ($a_{max} = 0.2$) make training more stable, while narrower bounds on action space ($a_{max} = 0.1$) allow for achieving a lower average episode length. We choose the best performing variant, namely, $a_{max} = 0.1$ with the target entropy T_E = -12 for the ablation study.

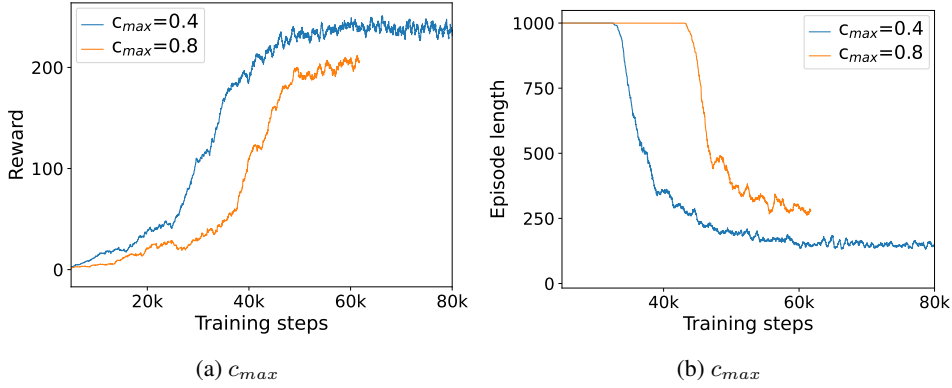


Figure 8: Performance comparison of MACS with different values of c_{max} .

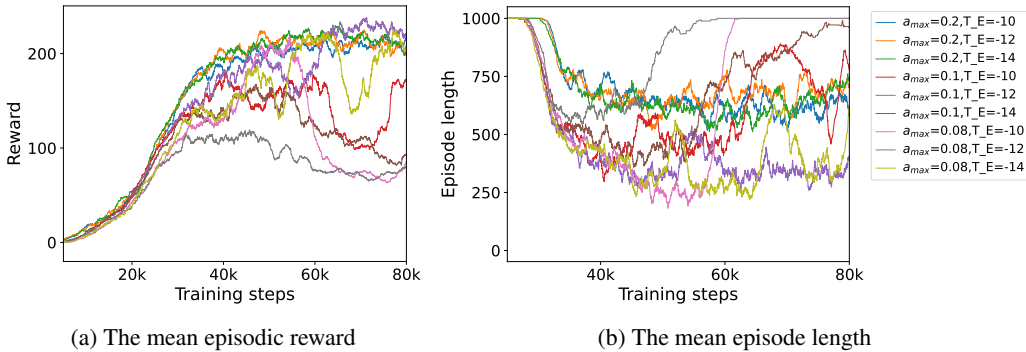


Figure 9: Performance comparison of MACS with different action space bounds and target entropy values.

A.5 Other hyperparameters

The list of hyperparameters used to train MACS is shown in Table 4. Figs. 10 and 11 show the mean episodic reward and the mean episode length achieved by MACS during training for different variations of the hyperparameters. We can see that the training batch size (Figs. 10c and 10d) and the entropy learning rate (Figs. 11c and 11d) play a crucial role.

Table 4: Hyperparameters used to train MACS.

Hyperparameter	value
γ	0.995
Training batch size	8192
Target entropy	-8
Truncate episodes	TRUE
Target network update frequency	1000
Number of samples before learning starts	500
Tau	0.001
Initial alpha	1
Use twin q	TRUE
Actor learning rate	0.0003
Critic learning rate	0.0003
Entropy learning rate	0.0001
Replay buffer capacity	10000000
Use prioritised replay buffer	FALSE
g_{max}	5
c_{max}	0.4
Observation component-wise normalization	TRUE
Number of nearest neighbors k	12
Max steps in episode	1000

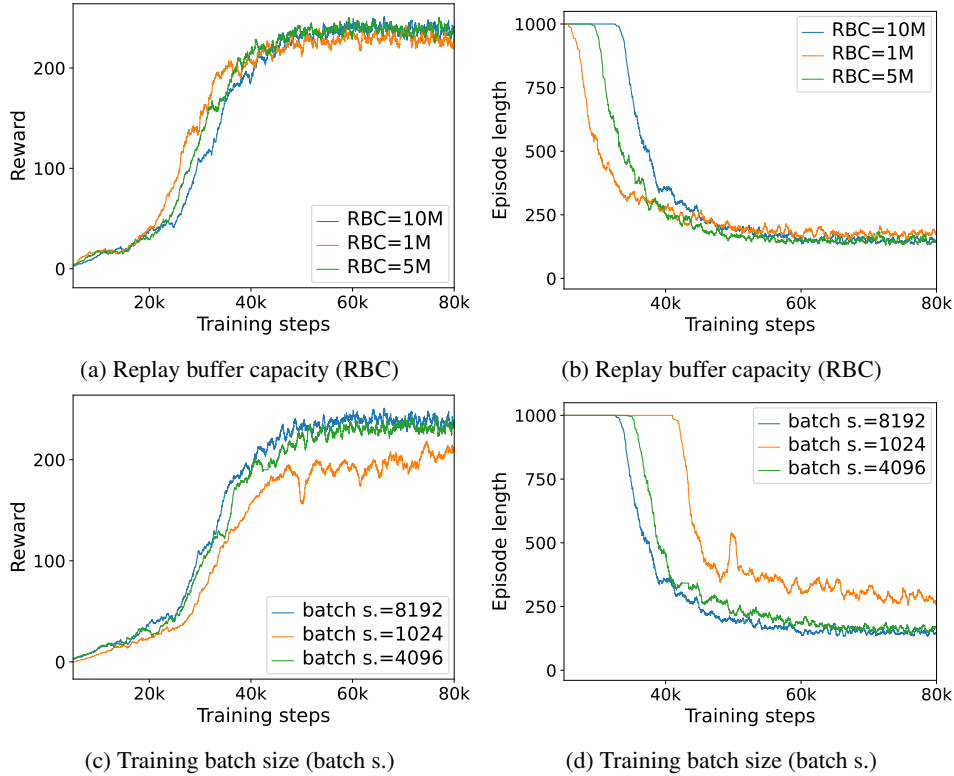


Figure 10: Performance comparison of MACS with different values of the replay buffer capacity and training batch size. The blue lines always indicate the values used in the paper.

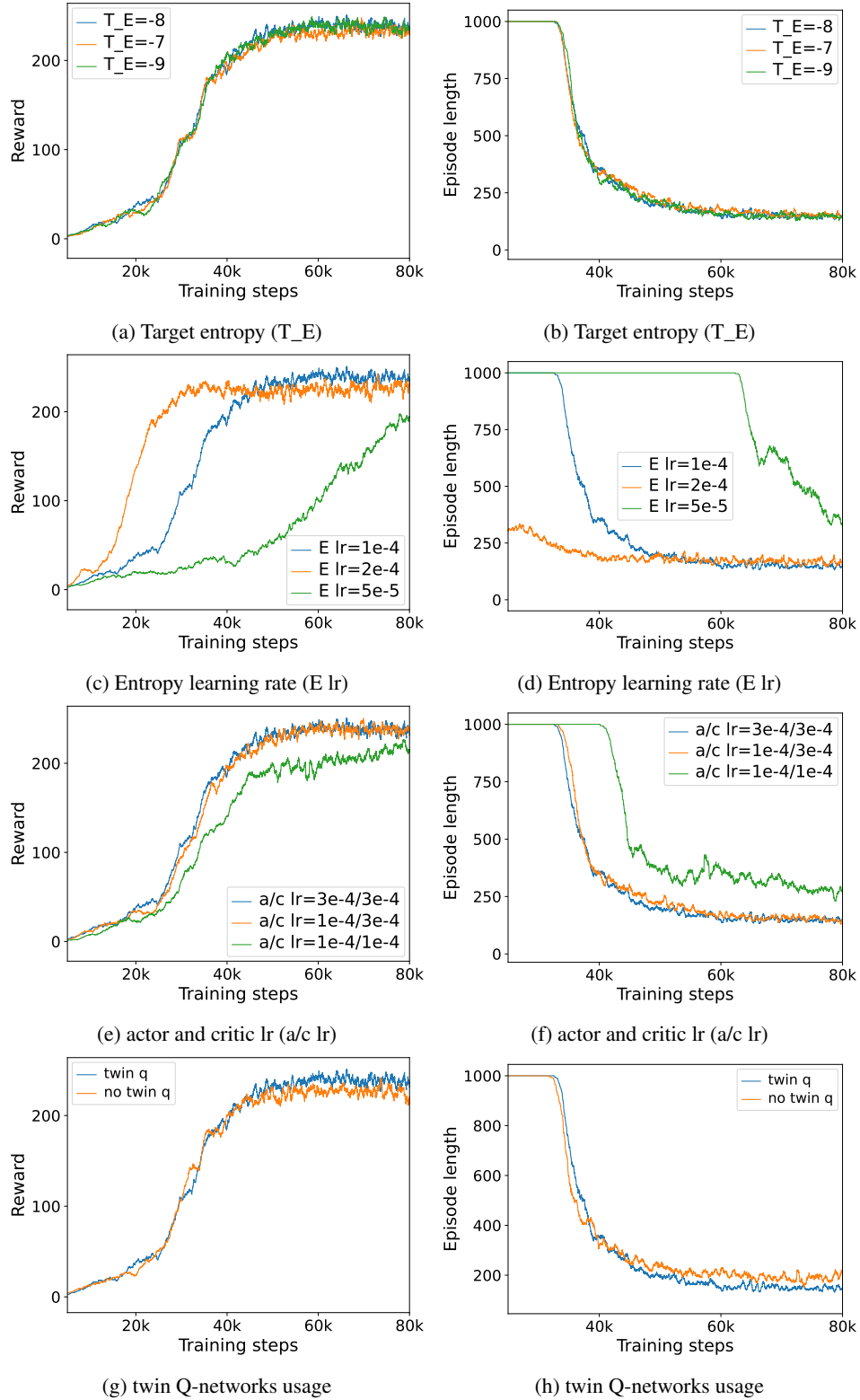


Figure 11: Performance comparison of MACS with different values of the target entropy, entropy/actor/critic learning rates, and twin Q-networks flag. The blue lines always indicate the values used in this study.

B Additional experimental details and results

B.1 Hardware usage for the training and testing purposes

We train MACS for ~ 80000 training steps in total using 40 concurrently running environments on a Linux cluster node equipped with two 20-core Intel(R) Xeon(R) Gold 6138 CPUs (2.00 GHz) and 384 GB of memory. All baselines are not data-driven or trained; they are based on explicit, deterministic logic.

Optimization of the test sets using MACS and the baselines was performed on the same hardware used to train MACS. However, only a single CPU core was used for the optimization of the test sets, while the remaining 39 cores remained idle. This setup was chosen to ensure a fair comparison by preventing MACS from gaining an advantage through parallelization, as the baselines are not parallelized.

B.2 Baselines

The baselines are accessed through the CHGNet package, which in turn interfaces with the optimization methods provided by the ASE package. We use the BFGS, BFGSLS, FIRE, and MDMin implemented in ASE, while CG is implemented in SciPy and accessed through the CHGNet \rightarrow ASE chain. The hyperparameters of the baselines are well-tuned and commonly used without modification; we adopt them as-is.

B.3 Random structures generation

We generate training and testing structures in the following way. Given a composition, a number of atoms, and a parameter v , we use the AIRSS package to generate a pseudo-random structure. AIRSS creates a unit cell with a random volume in the range $[v - 5\%, v + 5\%]$ and places the atoms within this unit cell so that the minimum distance between any two atoms is 1Å.

During training, at the beginning of each episode, we randomly select a composition from the list of training compositions. We use the volume of the experimental structure for a given composition as the parameter v in both training and testing to reflect the physics of the real material. Another parameter is the number of atoms in a structure, which is selected to be closest to 40 atoms, given the composition.

B.4 Additional experiment results

Table 5 compares MACS and all baselines in terms of T_{mean} (with standard errors) across all test sets. Table 6 compares MACS and all baselines in terms of N_{mean} and C_{mean} (with standard errors) across all test sets. Table 7 shows P_F for all test sets and methods. Figs. 12 and 13 show the energy distribution for the local minima obtained by the different methods for all test sets. Figs. 14 and 15 show the energy evolution averaged by all successful optimizations of all test sets by the different methods.

Table 5: Comparison of MACS and the baselines by T_{mean} on all test sets. Standard errors are in brackets.

Composition	N atoms	T_{mean} (sec)						
		MACS	BFGS	FIRE	MDMin	BFGSLS	FIRE+BFGSLS	CG
Y ₂ O ₃	40	18(1)	48(2)	42(2)	74(2)	28(2)	38(2)	64(4)
	60	32(1)	85(3)	92(3)	155(3)	70(7)	74(2)	118(6)
	80	48(1)	137(4)	130(4)	207(4)	97(7)	112(4)	184(9)
Cu ₂₈ S ₁₆	44	29(1)	62(2)	47(1)	116(3)	54(12)	47(1)	81(3)
	66	51(1)	112(3)	88(2)	205(4)	60(1)	79(2)	147(5)
	88	74(2)	175(4)	120(2)	315(4)	110(2)	117(2)	275(7)
SrTiO ₃	40	57(12)	94(3)	109(3)	248(5)	65(5)	102(1)	134(7)
	60	90(12)	163(6)	202(5)	461(6)	138(10)	200(21)	250(13)
	80	142(13)	242(8)	366(8)	672(7)	214(16)	332(17)	452(20)
Ca ₃ Ti ₂ O ₇	48	59(12)	135(5)	119(3)	264(5)	68(3)	120(4)	156(7)
	72	106(12)	199(6)	239(4)	479(7)	184(18)	252(5)	301(14)
	96	163(12)	276(7)	412(14)	705(7)	195(6)	324(13)	499(21)
K ₃ Fe ₅ F ₁₅	46	31(1)	82(3)	124(5)	155(3)	68(5)	98(6)	132(7)
	69	51(1)	146(4)	214(8)	276(5)	118(19)	181(16)	248(11)
	92	96(12)	236(6)	377(12)	485(8)	154(9)	271(17)	371(16)
Ca ₃ Al ₂ Si ₃ O ₁₂	40	117(4)	127(5)	226(7)	585(5)	167(23)	190(5)	307(17)
	60	237(14)	266(8)	389(14)	1068(7)	276(16)	422(13)	572(31)
	80	343(16)	333(8)	627(18)	1279(6)	400(7)	627(17)	958(47)
Compositions unseen during training								
Sr ₂ TiO ₄	56	65(2)	145(5)	174(5)	361(5)	105(10)	139(2)	234(12)
	112	189(13)	358(10)	665(18)	759(6)	414(63)	440(8)	559(23)
Sr ₃ Ti ₂ O ₇	48	54(1)	123(4)	151(4)	315(5)	88(6)	130(1)	191(9)
	96	159(12)	369(10)	497(10)	800(6)	366(65)	375(6)	477(20)
Sr ₄ Ti ₃ O ₁₀	34	30(1)	77(3)	87(3)	174(4)	48(3)	76(3)	106(6)
	68	113(12)	202(6)	238(6)	498(7)	149(23)	205(4)	307(16)

Table 6: Comparison of MACS and the baselines by N_{mean} and C_{mean} on all test sets. The metrics N_{mean} and C_{mean} are presented either as a single value (if they are identical) or separated by a ; symbol (if they differ). Standard errors are in the brackets.

Composition	N atoms	$N_{\text{mean}} ; C_{\text{mean}}$						
		MACS	BFGS	FIRE	MDMin	BFGSLS	FIRE+BFGSLS	CG
Y ₂ O ₃	40	121(3)	313(10)	262(4)	442(11)	137(2); 185(7)	252(3); 267(6)	122(2); 543(10)
	60	147(3)	340(10)	338(5)	553(12)	178(5); 281(23)	324(4); 357(9)	145(3); 642(12)
	80	169(3)	395(10)	393(4)	625(14)	206(5); 307(20)	360(5); 403(14)	171(3); 754(15)
Cu ₂₈ S ₁₆	44	150(3)	293(6)	257(4)	543(11)	147(3); 177(6)	232(3); 242(3)	158(3); 716(13)
	66	186(4)	355(8)	307(5)	633(11)	176(3); 201(4)	280(3); 291(4)	198(4); 881(20)
	88	230(5)	414(7)	392(6)	745(12)	213(4); 239(4)	352(3); 365(4)	283(6); 1269(26)
SrTiO ₃	40	143(3)	255(8)	314(5)	625(12)	133(3); 190(16)	276(2); 299(3)	141(3); 572(13)
	60	179(4)	316(10)	379(6)	719(14)	169(3); 255(14)	321(3); 406(48)	168(4); 681(16)
	80	208(5)	329(8)	446(7)	765(17)	199(4); 317(26)	355(3); 433(24)	205(5); 837(21)
Ca ₃ Ti ₂ O ₇	48	146(3)	270(9)	324(5)	623(13)	136(2); 185(10)	284(2); 317(11)	151(3); 618(12)
	72	183(4)	310(8)	408(6)	707(15)	168(3); 249(27)	335(3); 374(7)	186(3); 756(12)
	96	205(4)	353(9)	467(6)	762(18)	193(3); 267(9)	369(3); 447(23)	213(4); 876(15)
K ₃ Fe ₅ F ₁₅	46	111(2)	274(8)	246(3)	501(10)	135(3); 178(7)	246(4); 263(6)	134(3); 602(16)
	69	128(2)	320(7)	293(4)	596(11)	163(4); 259(53)	299(5); 344(28)	160(3); 720(12)
	92	143(2)	359(6)	326(4)	642(10)	176(4); 236(13)	353(5); 396(16)	181(4); 815(20)
Ca ₃ Al ₂ Si ₃ O ₁₂	40	209(5)	189(5)	307(6)	700(31)	141(4); 264(46)	269(3); 311(6)	147(4); 553(15)
	60	264(7)	230(5)	382(6)	755(55)	165(3); 296(16)	316(3); 391(14)	177(4); 669(15)
	80	317(8)	246(6)	461(7)	894(0)	189(3); 327(6)	350(3); 458(16)	214(6); 814(23)
Compositions unseen during training								
Sr ₂ TiO ₄	56	172(4)	335(10)	371(6)	700(14)	162(3); 218(7)	319(3); 353(6)	175(4); 716(15)
	112	245(5)	420(10)	554(8)	850(16)	242(5); 397(35)	427(4); 508(10)	245(4); 1003(19)
Sr ₃ Ti ₂ O ₇	48	153(4)	288(8)	345(5)	676(12)	153(3); 210(10)	299(2); 323(3)	167(4); 682(17)
	96	227(5)	382(9)	501(7)	817(20)	212(4); 343(31)	385(3); 449(7)	223(5); 909(19)
Sr ₄ Ti ₃ O ₁₀	34	126(3)	251(8)	282(5)	547(13)	124(3); 173(14)	256(3); 275(3)	137(4); 557(17)
	68	186(5)	310(8)	408(6)	729(14)	179(4); 304(62)	339(3); 385(8)	183(3); 743(14)

Table 7: Comparison of MACS and the baselines by P_F (%).

Composition	N atoms	MACS	BFGS	FIRE	MdMin	BFGSLS	FIRE+BFGSLS	CG
Y ₂ O ₃	40	0.33	5.67	7	17.33	0.33	1.33	19
	60	0	4.33	16	28.67	1	0.67	26.67
	80	0.67	12.67	18.33	39.33	0.33	1.33	32.33
Cu ₂₈ S ₁₆	44	0.33	3.67	1	4	0.67	0	6.67
	66	0.33	2.67	2.67	15	0	0	11
	88	0	0	0.33	56.67	0	0	3.33
SrTiO ₃	40	0	2.33	3.33	25	0	0.33	15.67
	60	0.33	2.33	5	46.33	0.67	0.67	21
	80	0.33	3	9.33	71.67	0.33	1.33	26.67
Ca ₃ Ti ₂ O ₇	48	0	3.67	1.33	22.33	0	0	10.33
	72	0	0.67	1.67	54	0.33	0.33	13
	96	0.33	0.67	3.33	72.33	0	0	20
K ₃ Fe ₅ F ₁₅	46	0	1.33	17.67	4.67	0.33	4.33	14
	69	0	1.33	22.67	14	0	3	19.33
	92	0	2.33	33.67	20.33	0.33	4	20
Ca ₃ Al ₂ Si ₃ O ₁₂	40	1	1.33	5	90	0	1	19
	60	3	1.33	3	97	0.33	0	24.33
	80	1.33	0	4.67	99.67	0	0.33	27
Compositions unseen during training								
Sr ₂ TiO ₄	56	0.33	3.33	14	46.33	1.33	0	17.67
	112	0	5.67	31	90	1.33	0	20.67
Sr ₃ Ti ₂ O ₇	48	0	2.67	4	38.33	0.33	0.33	17.67
	96	0	3.67	14	81.33	1	0	20.33
Sr ₄ Ti ₃ O ₁₀	34	0.33	5	4	18.67	0	0.67	14.67
	68	0	2.33	8.33	55.67	0	0	17

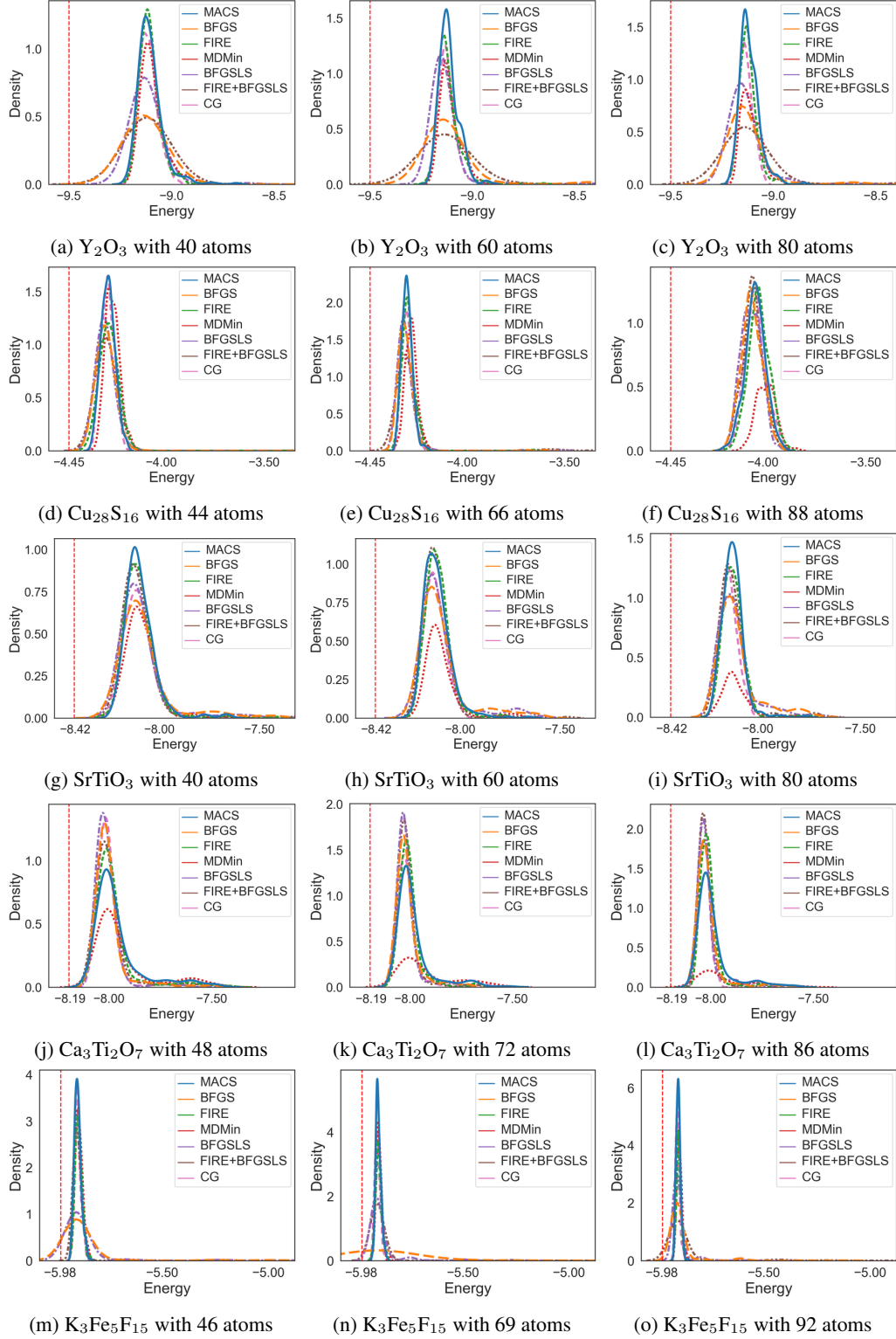


Figure 12: The energy distribution of the local minima obtained by all different methods. The vertical line indicates the energy of the experimental structure.

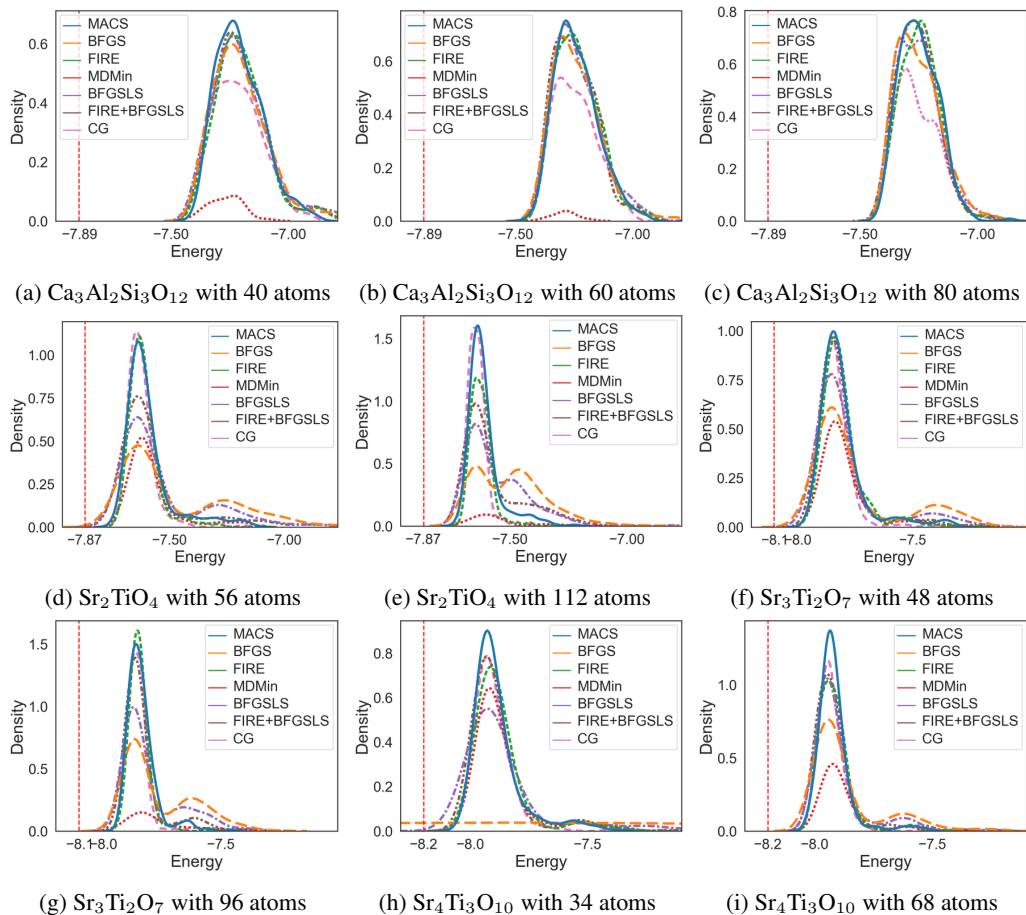


Figure 13: The energy distribution of the local minima obtained by all different methods. The vertical line indicates the energy of the experimental structure.

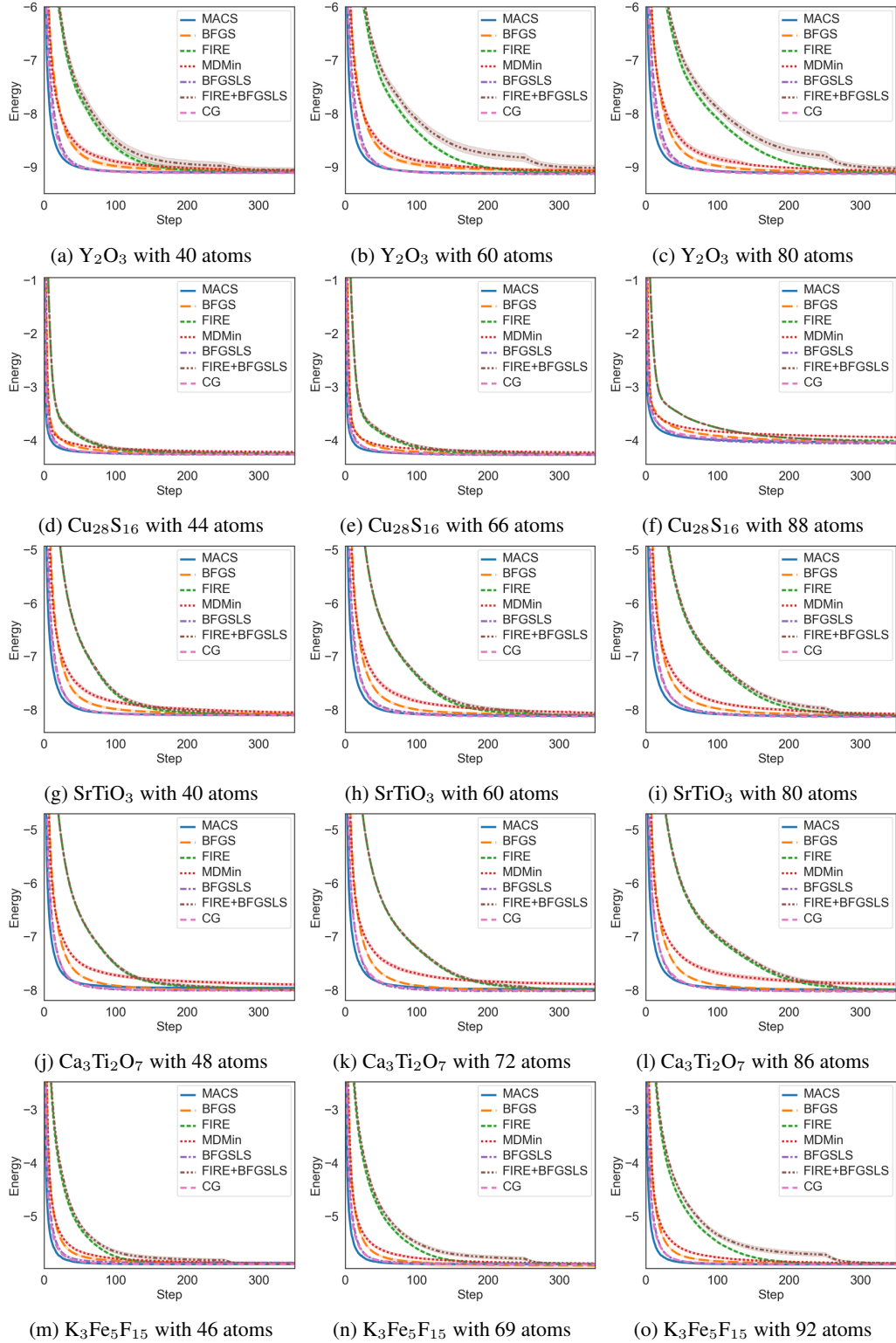


Figure 14: Energy evolution averaged over all successfully optimized structures for all methods on the given test set.

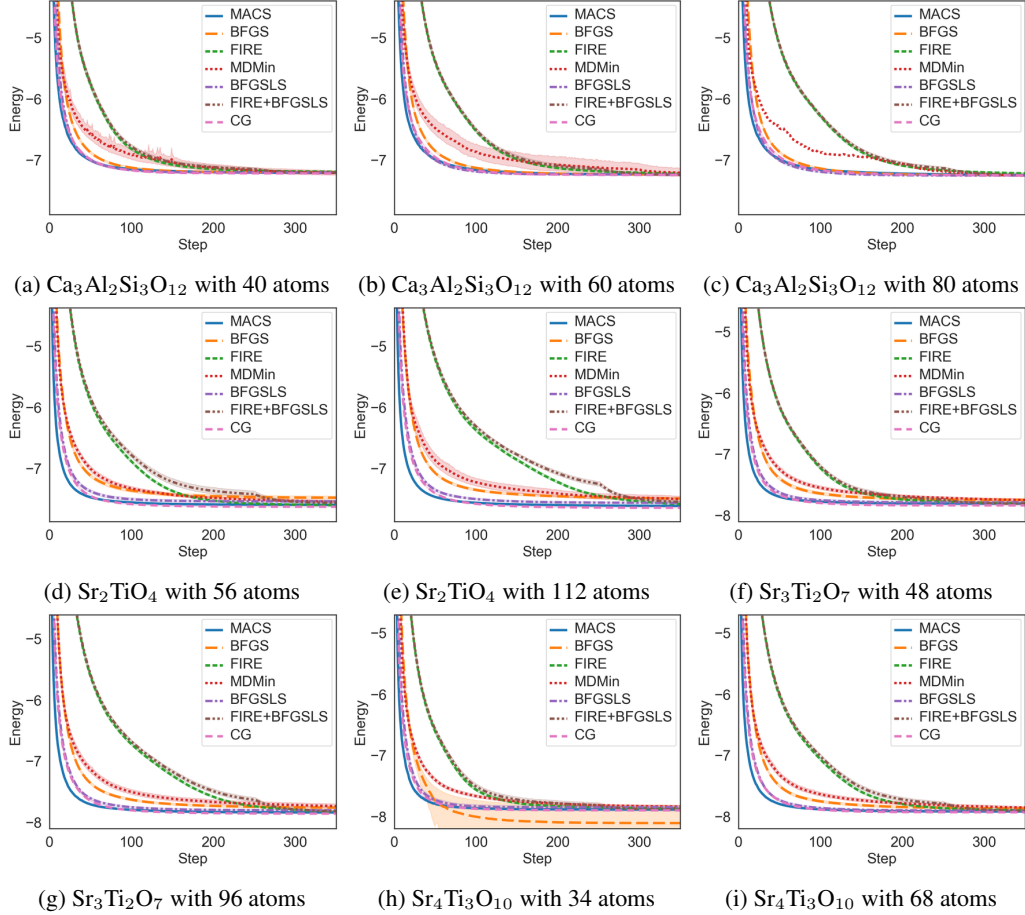


Figure 15: Energy evolution averaged over all successfully optimized structures for all methods on the given test set.

B.5 Composition targeted training

We train MACS on the only composition ($\text{Ca}_3\text{Al}_2\text{Si}_3\text{O}_{12}$) in which MACS was outperformed by a baseline (BFGS). We train the policy for the same period of time as we did for the cross-composition training. Table 8 confirms that MACS trained specifically on $\text{Ca}_3\text{Al}_2\text{Si}_3\text{O}_{12}$ structures is superior to BFGS and MACS trained across all compositions in the training set in all metrics. The composition $\text{Ca}_3\text{Al}_2\text{Si}_3\text{O}_{12}$ has the largest number of species, and its observation space can be more diverse than those of other compositions in this study. We suggest that longer training or increasing the proportions of complex compositions during training can help MACS optimize them better.

Table 8: Comparison of the MACS policy trained on the $\text{Ca}_3\text{Al}_2\text{Si}_3\text{O}_{12}$ composition (MACS individual) with the MACS policy trained across all compositions in the training set (MACS) and BFGS.

Composition	N atoms	T_{mean} (sec)			N_{mean}		
		MACS	MACS individual	BFGS	MACS	MACS individual	BFGS
$\text{Ca}_3\text{Al}_2\text{Si}_3\text{O}_{12}$	40	117	85	127	209	153	189
	60	237	170	266	264	205	230
	80	343	237	333	317	229	246
AVERAGE	60	232	164	242	264	196	222
P_F (%)		1.78	0.33	0.89			

B.6 Additional ablation study

Observations. MACS and feat.9 achieve similar mean episodic reward and mean episode length during training, as well as similar performance in optimizing SrTiO₃ structures. We proceed with the optimization of all test sets using the feat.9 design and compare the results of MACS and feat.9 in Table 9. We can see that the two policies are comparable in terms of T_{mean} , while MACS achieves an N_{mean} that is 7.7% lower than that of feat.9, confirming the superiority of MACS³.

Table 9: Comparison of the feat.9 design with MACS by T_{mean} and N_{mean} . Standard errors are in brackets.

Composition	N atoms	T_{mean} (sec)		N_{mean}	
		MACS	feat.9	MACS	feat.9
Y ₂ O ₃	40	18(1)	22(1)	121(3)	143(5)
	60	32(1)	39(1)	147(3)	168(4)
	80	48(1)	61(2)	169(3)	211(6)
Cu ₂₈ S ₁₆	44	29(1)	29(1)	150(3)	158(4)
	66	51(1)	54(2)	186(4)	214(6)
	88	74(2)	67(3)	230(5)	338(30)
SrTiO ₃	40	57(12)	44(1)	143(3)	145(3)
	60	90(12)	81(2)	179(4)	184(5)
	80	142(13)	132(3)	208(5)	209(4)
Ca ₃ Ti ₂ O ₇	48	59(12)	56(1)	146(3)	154(3)
	72	106(12)	98(2)	183(4)	183(4)
	96	163(12)	134(3)	205(4)	214(4)
K ₃ Fe ₅ F ₁₅	46	31(1)	38(1)	111(2)	141(3)
	69	51(1)	64(2)	128(2)	167(4)
	92	96(12)	112(2)	143(2)	183(4)
Ca ₃ Al ₂ Si ₃ O ₁₂	40	117(4)	111(3)	209(5)	189(5)
	60	237(14)	195(5)	264(7)	245(7)
	80	343(16)	334(8)	317(8)	292(7)
Compositions unseen during training					
Sr ₂ TiO ₄	56	65(2)	63(1)	172(4)	172(4)
	112	189(13)	174(4)	245(5)	247(5)
Sr ₃ Ti ₂ O ₇	48	54(1)	53(1)	153(4)	155(4)
	96	159(12)	159(4)	227(5)	229(5)
Sr ₄ Ti ₃ O ₁₀	34	30(1)	31(1)	126(3)	131(3)
	68	113(12)	88(2)	186(5)	190(4)
AVERAGE	66	100	101	181	195

³The optimization of the test set with the Cu₂₈S₁₆ structures of 88 atoms was interrupted by the cluster maintenance works and could not be finished due to the replacement of the hardware used for testing. Although optimization of the remaining structures of this test set could change the aggregated numbers, we rely on the comparison between all test sets to conclude that MACS consistently outperforms feat.9 as it consistently requires a lower number of energy calculations than feat.9.